The dimeric architecture of checkpoint kinases Mec1^{ATR} and Tel1^{ATM} reveal a common structural organisation

Marta Sawicka[1,5], Paulina H. Wanrooij[2,3,5], Vidya C. Darbari[1,5], Elias Tannous[2], Sarem Hailemariam[2], Daniel Bose[1,4], Alena V. Makarova[2], Peter M. Burgers[2,6] and Xiaodong Zhang[1,6]

[1]Section of Structural Biology, Department of Medicine, Imperial College London, South Kensington, London, UK
[2]Department of Biochemistry and Molecular Biophysics, Washington University School of Medicine, St Louis, Missouri, USA
[3]Current address: Department of Medical Biochemistry and Biophysics, Umeå University, Umeå, Sweden
[4]Current address: Perelman School of Medicine, University of Pennsylvania, Philadelphia, Pennsylvania, USA
[5]Joint first authors
[6]Joint corresponding authors

Running title: *Structural organisation of Mec1-Ddc2 and Tel1*

Contact information: Xiaodong Zhang, xiaodong.zhang@imperial.ac.uk, +44 (0) 207-594-3151
Peter Burgers, burgers@biochem.wustl.edu, +01 314-362-3872

Keywords: ATR, ATM, PIKKs, DNA damage response, Checkpoint signalling

ABSTRACT

The phosphatidylinositol 3-kinase-related protein kinases (PIKKs) are key regulators controlling a wide range of cellular events. The yeast Tel1 and Mec1-Ddc2 complex (ATM and ATR-ATRIP in humans) play pivotal roles in DNA replication, DNA damage signalling and repair. Here, we present the first structural insight for dimers of Mec1-Ddc2 and Tel1 using single particle electron microscopy. Both kinases reveal a head-to-head dimer with one major dimeric interface through their N-terminal HEAT repeats. Their dimeric interface is significantly distinct from the interface of mTOR Complex 1 dimer, which oligomerises through two spatially separate interfaces. We also observe different structural organisation of kinase domains of Mec1 and Tel1. The kinase domains in the Mec1-Ddc2 dimer are located in close proximity to each other. However, in the Tel1 dimer they are fully separated providing potential access of substrates to this kinase, even in its dimeric form.

INTRODUCTION

Mec1 (yeast orthologue of mammalian ATR - *Ataxia Telangiectasia* and Rad3-related) and Tel1 (yeast orthologue of ATM - *Ataxia Telangiectasia*-Mutated) belong to the phosphatidylinositol 3-kinase-related protein kinase (PIKK) family that control a plethora of cellular events including DNA damage response, DNA replication, growth control and mRNA surveillance. Other members of the PIKK family include mammalian DNA-PKcs, mTOR (Tor1 and Tor2 in yeast), TRRAP and SMG-1 (1,2). PIKKs have a conserved domain architecture consisting of the FAT domain (named after their members FRAP, ATM and TRRAP), kinase domain and FATC (FRAP, ATM and TRRAP C-terminus) domain at the C-terminus, as well as HEAT (named after Huntingtin, elongation factor 3 (EF3), protein phosphatase 2A (PP2A), and the yeast kinase TOR1) repeats of variable lengths at the N-terminus.

Due to the large size of these proteins, ranging from 2,368 amino acids for Mec1 to 4,128 amino acids for DNA-PKcs, these proteins are difficult to be purified in large quantities, thus hindering biochemical and structural analysis. There are a number of low-resolution electron microscopy reconstructions available. These include a monomeric ATM with and without DNA bound at 30 Å resolution (3), dimeric ATM at 26 Å (4), DNA-PKcs with and without DNA bound as well as DNA-bound DNA-PKcs/Ku70/Ku80 complex,

all at around 30 Å (5,6), DNA-PKcs at 13 Å and 7 Å (7,8), SMG-1 in complex with SMG-9 at 24 Å (9), SMG-1-UPF complexes (SMG-1:SMG-8:SMG-9 complex with UPF1 or UPF2) at a range of 17 Å to 22 Å (10,11), mTOR complex 1 structure at 26 Å (12) and TOR complex 2 structure at 26 Å (13). The crystal structure of DNA-PKcs at 6.6 Å (14) provided the first medium-resolution structural information on a full length PIKK. Although not all regions are resolved, the structure reveals the large array of HEAT repeats arranged in a circular fashion, enclosing a large channel. Very recently, the crystal structure of the C-terminal domain of mTOR, containing the conserved FAT, kinase and FATC regions was determined at 3.2 Å followed by the cryo-electron microscopy structure of the human mTOR complex 1 (mTORC1) at 5.9 Å revealing the dimeric organisation of these domains (15,16). Although the PIKKs feature a conserved amino acid sequence of the common domains, the known structures of monomers and dimers do not explain the precise domain organisations in a three-dimensional space for the various PIKKs. Furthermore, certain PIKKs such as ATM are believed to be active as monomers (17), whereas the mTOR structures reveal active dimers (13,16).

In budding yeasts, Mec1 and Tel1 are apical enzymes in DNA damage checkpoint pathways. They detect DNA damage and temporarily halt cell cycle progression while elevating and activating DNA repair proteins (18-21). Mec1 and Tel1 phosphorylate numerous target proteins involved in cell cycle, DNA repair and replication including Rad53, Chk1, Ddc1-Rad17-Mec3 (9-1-1 checkpoint clamp), Replication Protein A (RPA) and Rad51 (22-26). Furthermore, Mec1 and Tel1 also play important roles in telomere maintenance (27,28). Current models suggest that Tel1 is recruited to double-stranded DNA (dsDNA) ends, while Mec1 is recruited to RPA-coated single-stranded DNA (ssDNA), generated either by end-resection during the DNA double-strand break repair or during replication fork reversal (25,29). Mec1 and Tel1 show all the domains characteristic of PIKKs including a PRD (PIKK regulatory domain) at the C-terminus but lack a distinct FRB (FKBP12-rapamycin binding) domain acting as a recruitment module (30). The PRD domain is sandwiched between the kinase and FATC domains and is an essential regulatory element in ATR and ATM (31). The FATC domain is very well conserved and absolutely essential for kinase activity (31). It has been proposed to be the site for protein interactions and localisation to damage sites (31). Tel1 contains an additional conserved N-terminal motif called TAN (Tel1/ATM N-terminal motif) that is important for telomere length maintenance and checkpoint signalling (32).

Similar to ATR, which forms a constitutive complex with its partner ATRIP, Mec1 also forms an integral complex with Ddc2 (also called Lcd1, Pie1) (33-35). This interaction is coordinated by the C-terminus of Ddc2 and the N-terminus of Mec1 (35,36). The N-terminal domain of Ddc2 has a coiled-coil domain important for oligomerization (37,38) followed by a region involved in interactions with checkpoint activators like Dpb11 (mammalian TopBP1) (31,39). The N-terminal domain of Ddc2 also features an acidic stretch that recognises RPA, thereby recruiting ATR-ATRIP$^{Mec1\text{-}Ddc2}$ complexes to ssDNA (40). Remarkably, ATRIP^{Ddc2} interaction partners like TopBP1^{Dpb11} and RPA also interact with the kinase domain of ATR^{Mec1} via contacts with the PRD or FATC regions (31,41). A structure of Mec1-Ddc2 is thus required to understand how Mec1 and Ddc2 can coordinate various interactions important for Mec1 function.

The activation of Mec1-Ddc2$^{ATR\text{-}ATRIP}$ complex and Tel1^{ATM} is tightly regulated. Post-translational modifications such as acetylation in ATM (42) and autophosphorylation in ATM and ATR (17,43) are shown to play important roles in activation. Activator proteins have been identified to substantially enhance mammalian PIKKs kinase activities such as TopBP1 for ATR-ATRIP and the Mre11-Rad50-Nbs1 (MRN) complex for ATM (31,44). Yeast Mec1-Ddc2 has a number of cell cycle-dependent activators, with the 9-1-1 clamp activating Mec1-Ddc2 in the G1 phase, Dpb11 together with the 9-1-1 clamp in the G2 phase, while Dna2, Dpb11 as well as the 9-1-1 clamp act in the S phase (45-48). Conserved hydrophobic residues in unstructured tails of the activator proteins are involved in bringing about the activation in Mec1-Ddc2 (49).

The precise activation mechanism is still unclear for both ATR^{Mec1} and ATM^{Tel1}, especially whether oligomerization plays a role in activation. For ATR-ATRIP, oligomerization of the ATRIP

subunits is essential for activation (37,38). However, ATM is proposed to undergo a dimer to monomer transition as a part of the activation mechanism. ATM also exists as active dimers on activation during oxidative stress, however the dimers are formed by a disulphide bridge between the C-terminal FATC domains (50). Activation of both ATR and ATM is initiated by autophosphorylation, which has been proposed to happen *in trans* and hence might require the close association of both kinase domains (17,43).

In this work, we provide the first structural information for dimers of Mec1-Ddc2 and Tel1 obtained using electron microscopy. These structures reveal the conformation of Mec1-Ddc2 and Tel1 in their pre-activated states. Both Mec1-Ddc2 and Tel1 structures show head-to-head dimer coordinated by the N-terminal HEAT repeats. Individual monomers of both Mec1 and Tel1 show a characteristic arm region formed by the N-terminal HEAT repeats and a head region formed by the FAT-kinase-FATC domains. A comparison of the Mec1-Ddc2 dimer with the Tel1 dimer shows a large difference in the distance between the head domains within the dimer, which are fully separated in Tel1, but in close proximity in Mec1-Ddc2 complex.

EXPERIMENTAL PROCEDURES

Protein expression and purification - The Mec1-Ddc2 complex was expressed and purified as previously described (51) with some modifications. Mec1-Ddc2 complex tagged with an IgG binding domain (ZZ) was overexpressed in yeast from pBL904 and cells were harvested and lysed using buffer HEP^{300} (50 mM HEPES-KOH (pH 7.8), 300 mM KCl, 10 % glycerol, 1 mM EDTA, 0.1 % Tween-20, 0.02 % $C_{12}E_{10}$, 3 mM DTT, 5 mM reduced glutathione, 10 mM $NaHSO_3$, 10 µM pepstatin A, 2 mM benzamidine, 10 µM leupeptin, 1mM PMSF, 5 mM $NaPP_i$, 10 mM β-glycerophosphate, 1 mM α-naphtylic acid, 5 mM NaF; superscript designates mM NaCl). The cell lysate was adjusted to a pH of 7.4 and a conductivity corresponding to that of 200 mM KCl buffer, and was clarified by ultracentrifugation at 35,000 rpm for 1 h in a 45 Ti rotor (Beckman Coulter). The supernatant was incubated with IgG beads (IgG sepharose 6 Fast Flow, GE Healthcare) for 3 hours and subjected to four consecutive washes with buffer HEP^{250}, HEP^{300}, HEP^{300} supplemented with 10 mM Mg-acetate and 1 mM ATP, and HEP^{400}. Mec1-Ddc2 was cleaved with HRV 3C protease and eluted.

The GST-tagged Tel1 was overexpressed in yeast from pBL602 and purified as previously described (51) with some modifications. Cells were harvested and lysed in buffer HEP^{300} (60 mM HEPES-KOH (pH 7.8), 40 mM potassium phosphate (pH 7.8), 10 % glycerol, 300 mM KCl, 150 mM ammonium sulfate, 2 mM DTT, 0.1 % Tween-20, 0.01 % NP-40, 1 mM EDTA, 0.5 mM EGTA, 10 mM β-glycerophosphate, 1 mM α-naphtylic acid, 5 µM pepstatin A, 5 µM leupeptin, 3 mM $NaHSO_3$ and 2 mM benzamidine). Ammonium sulfate precipitated protein was resuspended in buffer HEP^0 and incubated with glutathione S-sepharose beads for 3 hours and subjected to four consecutive washes with buffer HEP^{100}, HEP^{100} lacking the protease and phosphatase inhibitors hereinafter, HEP^{100} supplemented with 10 mM Mg-Acetate and 1 mM ATP, and HEP^{100}. The GST-tagged Tel1 was cleaved by HRV 3C protease and further purified over a heparin column and eluted in HEP^{700}.

Gel filtration analysis - Mec1-Ddc2 was buffer-exchanged to 50 mM HEPES-KOH (pH 7.4), 200 mM KCl, 10 % glycerol, 0.1 % Tween-20, 0.01 % NP-40, 1 mM EDTA, 1 mM EGTA and 2 mM DTT using Amicon Ultra 0.5 columns (Merck Millipore) and run over a Superose 6 HR 10/30 gel filtration column (Pharmacia Biotech) at 0.3 ml/min. Tel1 was buffer-exchanged to 50 mM HEPES-KOH (pH 7.4), 200 mM KCl, 10 % glycerol, 0.1 % Tween-20, 0.02 % $E_{10}C_{12}$, 1 mM EDTA, and 3 mM DTT and run over a Superose 6 Increase 5/150 GL gel filtration column (GE Healthcare) at 0.1 ml/min. Elution was monitored at 280 nm and peak fractions were separated on an 8 % SDS-PAGE gel to verify protein identity. Migration of the Mec1-Ddc2 complex and Tel1 was compared to that of the gel filtration standards (#151-1901, Bio-Rad) in order to estimate the size of the complex.

Mec1 kinase activity assays - 10 nM Mec1-Ddc2 was incubated with 100 nM GST-Rad53-kd in 10 µl reactions containing 25 mM HEPES (pH 7.6), 100 mM NaCl, 8 mM Mg-acetate, 100 µg/ml BSA, 1 mM DTT, 100 µM ATP, 0.5 µCi [ɣ-P^{32}]-ATP and 50 nM Dpb11, where indicated.

Reactions were allowed to proceed for 10 min at 30°C and stopped by addition of 4 µl of 5 x SDS-PAGE loading dye. Samples were boiled for 5 min, separated on 8 % SDS-PAGE gels, dried and exposed to a phosphor screen (GE Healthcare).

Antibody labeling of Mec1-Ddc2 and Tel1 - 16 nM Mec1-Ddc2 complex was labeled with 32 nM goat anti-Mec1 FATC, yS-20, polyclonal antibody (Santa Cruz Biotechnology) in 10 µl reactions containing 30 mM HEPES-KOH (pH 7.4), 150 mM NaCl, 2.5 % glycerol, 0.25 mM EDTA and 0.5 mM DTT. 20 nM Tel1 was labeled with the same anti-FATC antibody at 40 nM in 25 µl reactions containing 50 mM HEPES-KOH (pH 7.4), 220 mM NaCl, 2 % glycerol, 1 mM EDTA, 0.5 mM EGTA, 1 mM DTT, 1mM $MgCl_2$, 0.02 % Tween-20, 0.002 % NP-40. The anti-Mec1, yS-20, antibody has been raised against the highly conserved C-terminal region of Mec1 (84% similarity with the Tel1 C-terminal region). The reactions were incubated on ice for 30 minutes before putting the labeled samples onto EM grids.

Negative stain electron microscopy data collection - 2 µl of 70 nM Mec1-Ddc2 (30 mM HEPES (pH 7.4), 200 mM NaCl, 5 % glycerol, 0.5 mM EDTA, 1 mM DTT), 2 µl of 20 nM Tel1 (50 mM HEPES (pH 7.4), 150 mM NaCl, 5 % glycerol, 1 mM EDTA, 1 mM DTT) and antibody-labeled samples at concentrations described above were deposited for 1 min on glow-discharged continuous carbon grids (TAAB, UK). The excess of liquid was blotted and a 2 µl drop of 2 % v/v uranyl acetate was added to the grids for 2 min. Excess of liquid were blotted and left to air dry. Mec1-Ddc2, Tel1 and the anti-Mec1 labeled complexes of Mec1-Ddc2 were imaged in a Philips CM200 electron microscope operating at 200 kV and equipped with a TVIPS slow scan 4k x 4k CCD camera. Micrographs were manually collected at a nominal magnification of 50,000 with a pixel size of 1.76 Å/pixel corresponding to an electron dose of 20 e/Å^2/s. All images were taken at a range of defocus from -2.5 to -3.5 µm. The antibody-labeled Tel1 sample was imaged in an FEI Tecnai F20 electron microscope operating at 200 kV and equipped with an FEI Falcon II CMOS Direct Electron Detection camera. Micrographs were manually collected at a nominal magnification of 62,000 corresponding to a pixel size of 1.65 Å/pixel and an electron dose of 32 e/Å^2/s.

Single particle negative stain image processing - 10,586 Mec1-Ddc2 and 7,350 Tel1 particles were picked using an e2boxer.py program of EMAN2 (52,53). Defocus and astigmatism parameters were estimated using CTFFIND3 (54). Mec1-Ddc2 and Tel1 data sets were used for *ab initio* reconstructions using a standard MSA/MRA (Multivariate Statistical Analysis/Multi Reference Alignment) routine in IMAGIC-V (55). Briefly, all particles were band-pass filtered with a 200 Å high-pass cutoff and a 10 Å low-pass cutoff and subjected to reference-free alignment. Class averages were generated using MSA allowing selecting distinctive classes, which were used as an initial reference set for MRA. Euler angles were manually assigned to three class averages along distinctive views. The assigned angles served as a set of angular references to determine Euler angles for all class averages and subsequently create an initial 3D model. Reprojections generated from the new model were used as a reference set to align particles and assign their orientation in 3D. Once the overall features of the Mec1-Ddc2 and Tel1 map were stabilized, two-fold symmetry (C2) was applied onwards. Further refinement for Mec1-Ddc2 was carried out in RELION-1.3 (56). Particles were subjected to reference-free 2D classification and subsequently reduced to 7,235 particles after removing poor quality particles. 3D reconstruction was generated by refining the Mec1-Ddc2 dimer model obtained using IMAGIC-V. The final reconstruction was obtained from 5,633 Mec1-Ddc2 particles at a resolution of 22.5 Å using the gold-standard FSC (0.143 criterion) (57). The Tel1 reconstruction was further refined using reprojections from the two-fold symmetrized model generated with IMAGIC-V and performing particle alignments and projection matching in SPIDER (58). Aligned particles were subjected to the MSA routine to generate class averages in IMAGIC-V. Angular assignments of the class averages generated from IMAGIC-V and back-projection for refining the structure was performed in SPIDER iteratively. The final reconstruction was obtained from the full dataset at a resolution of 21 Å (FSC=0.5 criterion). The model was further verified using RELION with the final reconstruction filtered to 40 Å that converged to

a 24 Å similar model in RELION using the gold-standard FSC (0.143 criterion).

Due to high heterogeneity of the antibody-labeled Mec1-Ddc2 and Tel1, individual particles with a clearly visible extra density were selected manually. 1,951 antibody labeled Mec1-Ddc2 particles were band-pass filtered with a 220 Å and a 20 Å cut-off and subjected to a reference-free alignment in IMAGIC-V. Centered particles were subjected to the MSA routine followed by 2D classification. 2D class averages that show a clear extra density were selected and compared with reprojections generated from the unlabeled model. 844 antibody-labeled Tel1 particles were also band-pass filtered with a 220 Å and a 20 Å cut-off. Visual inspection between the 2D class averages of anti-FATC Mec1-Ddc2/individual images of anti-FATC Tel1 particles and reprojections along the same Euler angles identified a number of antibody labeled particles that show an extra density corresponding to the anti-FATC antibody. Positions of the bound antibodies were identified using triangulation methods.

Electron cryo-microscopy data collection - Tel1 was diluted in a buffer optimized for cryo-freezing while preserving the protein stability and integrity. The final buffer included 50 mM HEPES-KOH (pH 7.4), 210 mM KCl, 1 % glycerol, 0.02 % Tween-20, 0.002 % NP-40, 1 mM EDTA, 0.5 mM EGTA, 1 mM DTT and 0.5 mM $MgCl_2$. Aliquots of 2 µl of Tel1 at a concentration of 20 nM were applied to glow-discharged holey carbon grids (Quantifoil Cu R2/2, 300 mesh) coated with an additional thin layer of carbon. After 30 second incubation in a humidity chamber at 4°C and 100 % relative humidity, the grids were blotted for 6 seconds and flash frozen in liquid ethane using an FEI Vitrobot Mark III. The grids were imaged in an FEI Tecnai F20 electron microscope operating at 200 kV and equipped with an FEI Falcon II CMOS Direct Electron Detection camera. Micrographs were manually collected at a nominal magnification of 62,000 corresponding to a pixel size of 1.65 Å/pixel and an electron dose of 32 e/$Å^2$/s. Images were recorded at a defocus ranging from -1 to -4 µm.

Electron cryo-microscopy image processing - All data were processed in RELION-1.4 (56). All the micrographs were corrected for CTF using CTFFIND3 (54). An initial dataset of 20,519 particles, selected using both manual and autopicking routine in RELION, was extracted after binning the particles twice giving the pixel size of 3.3 Å/pixel. References for autopicking were generated using the initial ~1,200 manually picked particles and performing a 2D classification routine. The dataset was further improved by multiple rounds of 2D classification to remove poor quality particles resulting in a reduced dataset of 17,226 particles. 3D classification was then employed to extract structurally homogenous data for 3D structure refinement. The negative stain-EM structure filtered to 60 Å was used as a starting model. The final dataset included 8,962 particles for refinement of the Tel1 structure. Iterative rounds of 3D classification protocol were used for refinement as described in the RELION tutorials for extremely difficult cases. Careful monitoring was carried out to avoid possible over-fitting and all interpretations of the structure have been carried out keeping this in mind. The final resolution estimated by this refinement protocol according to resolution estimates used in Bayesian approach (59) was 14.1 Å. A final round of refinement was then carried out for local refinement in Refine3D routine of RELION. The final reconstruction converged to a resolution of 19.2 Å using the gold-standard FSC (0.143 criterion).

Fitting of mTOR crystal structures and map segmentation - A 3.2 Å crystal structure of the C-terminal mTOR (PDB ID: 4JSV) without the FRB domain (residues 2021-2118) was docked into the EM density corresponding to the kinase domain of Mec1 and Tel1. A 5.9 Å atomic structure of mTOR (PDB ID: 5FLC) modeled into the cryo-EM map of mTORC1 (EMD-3213) was docked into the EM densities of the Mec1-Ddc2 complex and Tel1. Prior to fitting the densities corresponding to Raptor and mLST8 subunits as well as the FKBP protein were removed. The Mec1-Ddc2 and Tel1 3D maps were then segmented in Chimera (60) and the domain boundary was based on the molecular fitting.

RESULTS

Mec1-Ddc2 and Tel1 exist as higher order oligomers - Mec1-Ddc2 was previously shown to form a stable complex of 360 kDa using analytical ultracentrifugation (51). However, these studies were carried out at high salt

conditions (0.4 M KCl) in order to prevent aggregation. In this study, the protein was purified to high homogeneity with improved buffer conditions (Fig. 1A), and all the experiments have been carried out in physiological salt concentrations (100-200 mM KCl). We analysed Mec1-Ddc2 on a Superose 6 HR 10/30 size-exclusion column and interestingly we found that the majority of Mec1-Ddc2 elutes with a retention time corresponding to a complex of ~ 700 kDa, and is thus consistent with the molecular weight of the Mec1-Ddc2 dimer (720 kDa, Fig. 1B). Mec1 activity has been measured with *in vitro* kinase assays. The enhanced phosphorylation of Rad53 (with the active site mutated) and Rpa1 in the presence of Dpb11 was observed for the fraction containing the Mec1-Ddc2 dimer (Fig. 1B, inset). Therefore, we confirmed that Dpb11 could activate the oligomeric form of Mec1-Ddc2 used in our structural studies.

Tel1 was purified to high homogeneity (Fig. 1C), analysed on a Superose 6 Increase 5/150 GL size-exclusion column and eluted with a retention time corresponding to ~700 kDa, which is consistent with the molecular weight of a Tel1 dimer (640 kDa, Fig. 1D).

3D reconstruction of Mec1-Ddc2 dimer - In order to investigate the structural organisation of Mec1-Ddc2, we used single particle negative stained Electron Microscopy (EM) to generate the 3D model of the complex. Negative stained EM was selected due to relatively low sample concentration and poor contrast in cryo-EM. We observed two populations of particles that differed significantly in their sizes. The majority (81 %) was consistent with the size of Mec1-Ddc2 dimer of 720 kDa (Fig. 2A). Based on the eigenimage analysis in IMAGIC-V (55), dimeric images displayed a two-fold symmetry. Using angular reconstitution methodology implemented in IMAGIC-V, we obtained an *ab initio* 3D reconstruction of Mec1-Ddc2 dimer and iteratively refined the model imposing two-fold symmetry. The quality of model was assessed by a side-by-side comparison of the 2D class averages (CA) with their corresponding reprojections (RP) generated from the 3D model (Fig. 2B). The final negative stain Mec1-Ddc2 dimer model (Fig. 2C) was obtained from 5,633 particles. The distribution of Euler angles of all particles used in generating the C2 structure (Fig. 2D) covers all angular space. The 3D refinement of the model converged at 22.5 Å (Fig. 2E). The dimeric Mec1-Ddc2 reconstruction (Fig. 2C) is 175 Å tall, 215 Å wide and 115 Å thick, resembling a pretzel with tubular density encircling multiple cavities. We can clearly distinguish two regions, which have been referred to as the head and arm domain in ATM, DNA-PKcs and SMG-1 reconstructions (3,5,9). Here, the head domain occupies the upper globular density while the arm domain forms an elongated and curved shape and consisting of tubular density regions encircling a cavity (Fig. 2C left). The model reveals multiple interaction sites within the arm and the head domains. The arm of one monomer is intertwined with the arm of another monomer. Weak contacts are also observed between the two opposite head domains suggesting their auxiliary roles in dimer formation and stabilisation.

3D reconstruction of Tel1 - Tel1 samples were initially analysed using negative stained EM to build an initial model (Fig. 3). Single particles revealed a distinct two-fold symmetry indicating that Tel1 existed mainly as dimers in the protein preparations. The initial model was generated using a dataset of 7,350 particles using IMAGIC-V (55) and SPIDER (58). Reference-free alignments were carried during the initial stages of image processing and subsequently angular reconstitution was utilised in building and refining the 3D model. The quality of the model is assessed by the consistency between the class averages (CA) and corresponding reprojections (RP) (Fig. 3B). The final negative stained 3D model measures 185 Å tall, 230 Å wide and 105 Å thick (Fig. 3C).

Tel1 was subsequently vitrified in a buffer that was compatible for cryo-freezing and stability of the protein to perform cryo-EM analysis (Fig. 4A). An initial dataset of 20,519 particles was selected by a combination of manual and autopicking in RELION (56). Multiple rounds of 2D classification were used to remove poor quality particles resulting in a reduced dataset of 17,226 particles. 3D classification was used to extract structurally homogenous data for 3D structure refinements. The negative stained EM model filtered to 60 Å was used as the starting model. Extraction of particles from the best model led to the final dataset of 8,962 particles that was used to refine the Tel1 structure using the 3D classification protocol. A further local refinement resulted in a final model at a

resolution of 19.2 Å using the gold-standard FSC (0.143 criterion). The quality of the 3D reconstruction generated in RELION was assessed by comparing the class averages calculated in IMAGIC-V with the reprojections along the same angles, assigned in IMAGIC-V using references generated from the 3D model (Fig. 4B).

The cryo-EM Tel1 structure (Fig. 4C) overall resembles the negative-stain reconstruction (Fig. 3C). However it is taller (200 Å vs. 185 Å) and narrower (215 Å vs. 230 Å) when compared with the negatively stained model. This could be due to the stain procedure, which could cause flattening artefact. The Tel1 structure starkly resembles the overall Mec1-Ddc2 dimer architecture. Each monomer displays the characteristic domains of the PIKKs with the arm and the head region. However, the two head domains in Tel1 are fully separated by 35 Å in the narrowest region and enclose a cavity ~20 Å long and 125 Å wide. The Tel1 dimer structure displays no obvious steric hindrance for substrates to access the kinase domains.

Domain assignment in Mec1-Ddc2 and Tel1 - The 3D reconstructions of both Mec1-Ddc2 and Tel1 display the head domain that is similar to head regions in other PIKK structures, where the FAT-kinase-FATC domains reside. We have used an antibody against the FATC domain to locate the FATC within Mec1-Ddc2 and Tel1 particle. Individual particles were carefully selected based on visual inspection. Only those representing the anti-FATC labelled particle with additional density adjacent to it were selected. Subsequently we carried out the reference-free alignment and 2D classification. Comparisons of the class averages with the reprojections generated from the Mec1-Ddc2 reconstruction located an extra density that corresponds to the anti-FATC antibody (Fig. 5A). For antibody-labelled Tel1 data, due to the preferential orientation and the low antibody labelling efficiency, there were insufficient data for reliable 2D classification. However, due to the distinct front view, it is unambiguous that the anti-FATC antibody is located within the globular head domain (Fig. 5B). Thus the FATC domains in both Tel1 and Mec1-Ddc2 are located within the globular domain.

Fitting the crystal structure of the C-terminal mTOR (15) and the FAT-kinase-FATC domain of mTORC1 (16) into our EM models of Mec1-Ddc2 and Tel1 (Fig. 6B and 6C) further supports that the cradle-shaped density of the head region consist of the FAT, kinase domain and the FATC domain. Based on our molecular fitting, we could also suggest the possible location of the catalytic and activation loop within the cleft of the Mec1 and Tel1 kinase domain as shown for mTOR (Fig. 6D). The elongated tubular arm domains agree with the shape and the dimensions of the HEAT repeats, which dominate both the N-terminal domains of Tel1 and Mec1 as well as the majority of Ddc2. Upon fitting all domains of the full-length mTOR into the Mec1-Ddc2 model, we have observed an unassigned density extending from the N-terminal HEAT repeats of Mec1. This density also forms an elongated and tubular arm indicating it is a natural extension of the N-terminal Mec1 and therefore might correspond to the Ddc2 subunit. These tubular arm domains intertwine and form the dimer interface.

Comparison of Mec1-Ddc2 and Tel1 - Mec1-Ddc2 and Tel1 structures display a similar dimer arrangement with the dimer interface formed by the N-terminal HEAT repeats of Tel1 and Mec1, as well as Ddc2 in Mec1-Ddc2 (Fig. 6). Overall dimensions of these two models are also comparable. However, the clear tubular density encircling a cavity in the arm region of the Mec1-Ddc2 reconstruction is missing in Tel1 (Fig. 2C and Fig. 3C). Monomeric Mec1-Ddc2 has a molecular weight of 360 kDa compared to 320 kDa of Tel1 (Fig. 6A), thus it is likely that one of the tubular density in the Mec1-Ddc2 reconstruction (Fig. 2C left, Fig. 6B front view) accounts for Ddc2, as also concluded from our molecular fitting. Another striking difference between these two structures is the orientation of the head regions within the dimer. The two kinase domains are fully separated in Tel1 thereby suggest no impediment for substrate recruitment in this model. On the other hand, the individual kinase domains in Mec1 are in close proximity enclosing only a small cavity between the two domains.

DISCUSSION

Mec1 and Tel1 serve as key regulators of the DNA damage response. Together with other members of the PIKK family, they share a conserved domain arrangement of the N-terminal arrays of HEAT repeats followed by

the C-terminal globular kinase flanked with the FAT and FATC domains.

Our EM reconstructions of Mec1-Ddc2 and Tel1 reveal their dimeric architecture and provide the first structural insights supporting earlier biochemical findings on Mec1-Ddc2$^{ATR-ATRIP}$ and Tel1^{ATM}. Both models adopt a similar architecture with the head region comprising the FAT, kinase and FATC domains as well as the curved arm region consisting of large stretches of the N-terminal HEAT repeats. Our models are consistent with the 6.6 Å crystal structure of DNA-PKcs (14) as well as structures of other PIKKs such as SMG-1 (10). The DNA-PKcs structures show that the head region also consists of the kinase and FATC domain with additional HEAT repeats extending from the head domain and curving back onto it, encircling a large cavity. SMG1 is also shown to consist of a head region with a body comprising of tubular density that curves back towards the head domain. Although Mec1 exists in a complex with its obligatory binding protein Ddc2, it exhibits a similar structural organisation. The C-terminal Ddc2 is predicted to contain HEAT repeats. As Ddc2 interacts with the N-terminal Mec1, as previously reported biochemically (35), it might form a natural extension of N-terminal HEAT repeats of Mec1. Based on our fitting of the 5.9 Å atomic model of mTOR (Fig. 6B) into the EM density of the Mec1-Ddc2 dimer, there is a remaining unassigned density extending from the N-terminal HEAT repeats of Mec1 that could accommodate the Ddc2 subunit. Then similarly to DNA-PKcs and SMG-1, Ddc2 could possibly fold back into Mec1, positioning its N-terminus in close proximity to the head region of Mec1. All PIKKs thus stabilize their C-terminal catalytic domains by using extended HEAT repeats, either within the same polypeptide chain as in Tel1^{ATM} and DNA-PKcs or by merging with an additional polypeptide chain such as Ddc2^{ATRIP}.

Dimers of Mec1-Ddc2 and Tel1 represent a PIKK in a functional form that exhibits basal kinase activity prior to activation (Fig. 1B inlet). The oligomerization of ATR-ATRIP through the ATRIP coiled-coil region is required for localisation into foci of radiation induced damage sites as well as stalled replication forks (37,38). Ddc2 also contains a coiled-coil region and thereby likely contributes to the dimeric interface of Mec1-Ddc2. Our domain assignment of Mec1-Ddc2 (Fig. 6B) locates HEAT repeats at the dimeric interface. It is also seen in Tel1 structure that the HEAT repeats form the major dimer interface at the arm region (Fig. 6C). Similar findings have also been observed in the EM structures of mTORC1 (16) and TORC2 (13) and mutations within the HEAT repeats of Mec1 lead to defective DNA damage responses in the G_1/S and intra-S checkpoints (61). Interestingly, we found that the dimeric interactions via HEAT repeats are likely to be stabilised by close vicinity of the FAT domain. Our Mec1-Ddc2 reconstruction shows that the kinase domains could also contribute to the dimer interface, and could thus regulate substrate binding through the association or dissociation of the kinase domains without the requirement for a complete dissociation of the dimer. The recent cryo-EM reconstruction of mTORC1 (16) also shows a dimeric structure. The dimeric architecture is distinct from the one reported here. In Mec1-Ddc2 and Tel1, there is one major dimer interface, formed by HEAT repeats into a large intertwined density region. While in mTORC1, at least two distinct dimer interfaces form by HEAT repeats, encircling a large cavity (Fig. 6D). In mTORC1, the two kinase domains are located similarly to that of Mec1 and Tel1 although the active sites are facing away from the dimer interface (Fig. 6B, C and D). It is possible that depending on the number of HEAT repeats, different forms of dimerization exist for the PIKKs. Alternatively, the different dimeric forms observed in our work and in mTORC1 could represent different functional states of the PIKKs.

A number of the PIKKs were reported to autophosphorylate via residues in the C-terminal domain as a molecular switch for their kinase activity (17,43,62,63). Our reconstructions show that the two head domains can adapt very different conformations within the dimer, suggesting that one monomer can phosphorylate the adjacent monomer within the dimer. Upon DNA damage, ATM has been inferred to exist as a dimer in its inactive form, and dimer dissociation by autophosphorylation is associated with activation of kinase activity (17). However, in the presence of the oxidative stress ATM dimerizes via a disulphide bridge in the FATC region and compensates for the loss of the MRN-dependent activity (50). The

seemingly conflicting requirement for dimers is consistent with our results presented here. We show that kinase domains could contribute to the dimer interface but substrate binding and possibly activation does not necessarily require a complete dissociation of the dimer, which is formed primarily through the HEAT repeats. It is possible that phosphorylation might disrupt a subset of the dimer interface, thereby affecting the stability of the dimer, which could manifest in different oligomeric states *in vitro*.

Our data here suggest a putative model for Mec1 and Tel1. While dimerization through these HEAT repeats brings the kinase domains of Mec1-Ddc2 in close proximity, perhaps suggesting that activation may require the separation of these domains, in Tel1, the kinase domains are separated by 35 Å. Therefore, activation of these PIKKs may proceed through a more complex mechanism rather than a simple separation of the kinase domains. There are certain mechanistic advantages to maintaining the dimer through the HEAT repeats anchor while allowing possible repositioning and activation of the kinase domains. A dimer could increase the interaction surface with cofactors or support co-operativity to allow a more efficient recruitment. Furthermore, a complete dissociation of dimers to monomers would imply that in order to deactivate Mec1 or Tel1 or to recycle it for other activities, re-association into dimers would be required. A tethered dimer could ensure that it can be readily recycled between an inactive and an active state, allowing rapid multiple rounds of controlled activation/deactivation. However, understanding of the exact activation mechanisms requires structural and biochemical data on a reconstituted complex involving the PIKK bound to its activator.

ACKNOWLEDGMENTS

We thank T. Pape for his help with electron microscopy data acquisition, R. L. Perera and other members in XZ's group for input and useful discussions, and Carrie Stith for expert technical assistance with Mec1 expression and purification. This project is funded by the Wellcome Trust Senior Investigator Award WT/098412/Z/12/Z (to X.Z.) and NIH grant GM083970 (to P.B.). M.S. is funded by a BBSRC PhD studentship and P.W. by the Emil Aaltonen foundation and the Swedish Cultural Foundation in Finland.

CONFLICT OF INTEREST

The authors declare that they have no conflicts of interest with the contents of this article.

AUTHOR CONTRIBUTIONS

MS, VD, PW, ET, SH, DB designed and performed the experiments, MS, VD, PW, PB and XZ analysed the data. PB and XZ conceived and designed the study. MS, VD performed the majority of electron microscopy while DB collected initial negative stain EM data for Mec1-Ddc2 complex. PW, ET, AM, and SH purified the proteins and performed biochemical analysis. MS, VD, XZ and PB wrote the manuscript.

REFERENCES

1. Abraham, R. T. (2004) PI 3-kinase related kinases: 'big' players in stress-induced signaling pathways. *DNA repair* **3**, 883-887
2. Lempiainen, H., and Halazonetis, T. D. (2009) Emerging common themes in regulation of PIKKs and PI3Ks. *The EMBO journal* **28**, 3067-3073
3. Llorca, O., Rivera-Calzada, A., Grantham, J., and Willison, K. R. (2003) Electron microscopy and 3D reconstructions reveal that human ATM kinase uses an arm-like domain to clamp around double-stranded DNA. *Oncogene* **22**, 3867-3874
4. Lau, W. C., Li, Y., Liu, Z., Gao, Y., Zhang, Q., and Huen, M. S. (2016) Structure of the human dimeric ATM kinase. *Cell Cycle* **15**, 1117-1124
5. Boskovic, J., Rivera-Calzada, A., Maman, J. D., Chacon, P., Willison, K. R., Pearl, L. H., and Llorca, O. (2003) Visualization of DNA-induced conformational changes in the DNA repair kinase DNA-PKcs. *The EMBO journal* **22**, 5875-5882
6. Spagnolo, L., Rivera-Calzada, A., Pearl, L. H., and Llorca, O. (2006) Three-dimensional structure of the human DNA-PKcs/Ku70/Ku80 complex assembled on DNA and its implications for DNA DSB repair. *Molecular cell* **22**, 511-519
7. Rivera-Calzada, A., Maman, J. D., Spagnolo, L., Pearl, L. H., and Llorca, O. (2005) Three-dimensional structure and regulation of the DNA-dependent protein kinase catalytic subunit (DNA-PKcs). *Structure* **13**, 243-255
8. Williams, D. R., Lee, K. J., Shi, J., Chen, D. J., and Stewart, P. L. (2008) Cryo-EM structure of the DNA-dependent protein kinase catalytic subunit at subnanometer resolution reveals alpha helices and insight into DNA binding. *Structure* **16**, 468-477
9. Arias-Palomo, E., Yamashita, A., Fernandez, I. S., Nunez-Ramirez, R., Bamba, Y., Izumi, N., Ohno, S., and Llorca, O. (2011) The nonsense-mediated mRNA decay SMG-1 kinase is regulated by large-scale conformational changes controlled by SMG-8. *Genes & development* **25**, 153-164

10. Melero, R., Uchiyama, A., Castano, R., Kataoka, N., Kurosawa, H., Ohno, S., Yamashita, A., and Llorca, O. (2014) Structures of SMG1-UPFs complexes: SMG1 contributes to regulate UPF2-dependent activation of UPF1 in NMD. *Structure* **22**, 1105-1119
11. Deniaud, A., Karuppasamy, M., Bock, T., Masiulis, S., Huard, K., Garzoni, F., Kerschgens, K., Hentze, M. W., Kulozik, A. E., Beck, M., Neu-Yilik, G., and Schaffitzel, C. (2015) A network of SMG-8, SMG-9 and SMG-1 C-terminal insertion domain regulates UPF1 substrate recruitment and phosphorylation. *Nucleic Acids Res* **43**, 7600-7611
12. Yip, C. K., Murata, K., Walz, T., Sabatini, D. M., and Kang, S. A. (2010) Structure of the human mTOR complex I and its implications for rapamycin inhibition. *Molecular cell* **38**, 768-774
13. Gaubitz, C., Oliveira, T. M., Prouteau, M., Leitner, A., Karuppasamy, M., Konstantinidou, G., Rispal, D., Eltschinger, S., Robinson, G. C., Thore, S., Aebersold, R., Schaffitzel, C., and Loewith, R. (2015) Molecular Basis of the Rapamycin Insensitivity of Target Of Rapamycin Complex 2. *Molecular cell* **58**, 977-988
14. Sibanda, B. L., Chirgadze, D. Y., and Blundell, T. L. (2010) Crystal structure of DNA-PKcs reveals a large open-ring cradle comprised of HEAT repeats. *Nature* **463**, 118-121
15. Yang, H., Rudge, D. G., Koos, J. D., Vaidialingam, B., Yang, H. J., and Pavletich, N. P. (2013) mTOR kinase structure, mechanism and regulation. *Nature* **497**, 217-223
16. Aylett, C. H., Sauer, E., Imseng, S., Boehringer, D., Hall, M. N., Ban, N., and Maier, T. (2016) Architecture of human mTOR complex 1. *Science* **351**, 48-52
17. Bakkenist, C. J., and Kastan, M. B. (2003) DNA damage activates ATM through intermolecular autophosphorylation and dimer dissociation. *Nature* **421**, 499-506
18. Morrow, D. M., Tagle, D. A., Shiloh, Y., Collins, F. S., and Hieter, P. (1995) TEL1, an S. cerevisiae homolog of the human gene mutated in ataxia telangiectasia, is functionally related to the yeast checkpoint gene MEC1. *Cell* **82**, 831-840
19. Sun, Z., Fay, D. S., Marini, F., Foiani, M., and Stern, D. F. (1996) Spk1/Rad53 is regulated by Mec1-dependent protein phosphorylation in DNA replication and damage checkpoint pathways. *Genes & development* **10**, 395-406
20. Lydall, D., Nikolsky, Y., Bishop, D. K., and Weinert, T. (1996) A meiotic recombination checkpoint controlled by mitotic checkpoint genes. *Nature* **383**, 840-843
21. Santocanale, C., and Diffley, J. F. (1998) A Mec1- and Rad53-dependent checkpoint controls late-firing origins of DNA replication. *Nature* **395**, 615-618
22. Sanchez, Y., Desany, B. A., Jones, W. J., Liu, Q., Wang, B., and Elledge, S. J. (1996) Regulation of RAD53 by the ATM-like kinases MEC1 and TEL1 in yeast cell cycle checkpoint pathways. *Science* **271**, 357-360
23. Sanchez, Y., Bachant, J., Wang, H., Hu, F., Liu, D., Tetzlaff, M., and Elledge, S. J. (1999) Control of the DNA damage checkpoint by chk1 and rad53 protein kinases through distinct mechanisms. *Science* **286**, 1166-1171
24. Paciotti, V., Lucchini, G., Plevani, P., and Longhese, M. P. (1998) Mec1p is essential for phosphorylation of the yeast DNA damage checkpoint protein Ddc1p, which physically interacts with Mec3p. *The EMBO journal* **17**, 4199-4209
25. Brush, G. S., Morrow, D. M., Hieter, P., and Kelly, T. J. (1996) The ATM homologue MEC1 is required for phosphorylation of replication protein A in yeast. *Proceedings of the National Academy of Sciences of the United States of America* **93**, 15075-15080
26. Flott, S., Kwon, Y., Pigli, Y. Z., Rice, P. A., Sung, P., and Jackson, S. P. (2011) Regulation of Rad51 function by phosphorylation. *EMBO Rep* **12**, 833-839
27. Mills, K. D., Sinclair, D. A., and Guarente, L. (1999) MEC1-dependent redistribution of the Sir3 silencing protein from telomeres to DNA double-strand breaks. *Cell* **97**, 609-620
28. Moser, B. A., Chang, Y. T., Kosti, J., and Nakamura, T. M. (2011) Tel1ATM and Rad3ATR kinases promote Ccq1-Est1 interaction to maintain telomeres in fission yeast. *Nature structural & molecular biology* **18**, 1408-1413

29. Zou, L., and Elledge, S. J. (2003) Sensing DNA damage through ATRIP recognition of RPA-ssDNA complexes. *Science* **300**, 1542-1548
30. Rivera-Calzada, A., Lopez-Perrote, A., Melero, R., Boskovic, J., Munoz-Hernandez, H., Martino, F., and Llorca, O. (2015) Structure and Assembly of the PI3K-like Protein Kinases (PIKKs) Revealed by Electron Microscopy. *AIMS Biophysics* **2**, 36-57
31. Mordes, D. A., Glick, G. G., Zhao, R., and Cortez, D. (2008) TopBP1 activates ATR through ATRIP and a PIKK regulatory domain. *Genes & development* **22**, 1478-1489
32. Seidel, J. J., Anderson, C. M., and Blackburn, E. H. (2008) A novel Tel1/ATM N-terminal motif, TAN, is essential for telomere length maintenance and a DNA damage response. *Mol Cell Biol* **28**, 5736-5746
33. Paciotti, V., Clerici, M., Lucchini, G., and Longhese, M. P. (2000) The checkpoint protein Ddc2, functionally related to S. pombe Rad26, interacts with Mec1 and is regulated by Mec1-dependent phosphorylation in budding yeast. *Genes & development* **14**, 2046-2059
34. Rouse, J., and Jackson, S. P. (2000) LCD1: an essential gene involved in checkpoint control and regulation of the MEC1 signalling pathway in Saccharomyces cerevisiae. *The EMBO journal* **19**, 5801-5812
35. Wakayama, T., Kondo, T., Ando, S., Matsumoto, K., and Sugimoto, K. (2001) Pie1, a protein interacting with Mec1, controls cell growth and checkpoint responses in Saccharomyces cerevisiae. *Mol Cell Biol* **21**, 755-764
36. Ball, H. L., Myers, J. S., and Cortez, D. (2005) ATRIP binding to replication protein A-single-stranded DNA promotes ATR-ATRIP localization but is dispensable for Chk1 phosphorylation. *Mol Biol Cell* **16**, 2372-2381
37. Ball, H. L., and Cortez, D. (2005) ATRIP oligomerization is required for ATR-dependent checkpoint signaling. *J Biol Chem* **280**, 31390-31396
38. Itakura, E., Sawada, I., and Matsuura, A. (2005) Dimerization of the ATRIP protein through the coiled-coil motif and its implication to the maintenance of stalled replication forks. *Mol Biol Cell* **16**, 5551-5562
39. Mordes, D. A., Nam, E. A., and Cortez, D. (2008) Dpb11 activates the Mec1-Ddc2 complex. *Proceedings of the National Academy of Sciences of the United States of America* **105**, 18730-18734
40. Ball, H. L., Ehrhardt, M. R., Mordes, D. A., Glick, G. G., Chazin, W. J., and Cortez, D. (2007) Function of a conserved checkpoint recruitment domain in ATRIP proteins. *Mol Cell Biol* **27**, 3367-3377
41. Nakada, D., Hirano, Y., Tanaka, Y., and Sugimoto, K. (2005) Role of the C terminus of Mec1 checkpoint kinase in its localization to sites of DNA damage. *Mol Biol Cell* **16**, 5227-5235
42. Sun, Y., Xu, Y., Roy, K., and Price, B. D. (2007) DNA damage-induced acetylation of lysine 3016 of ATM activates ATM kinase activity. *Mol Cell Biol* **27**, 8502-8509
43. Liu, S., Shiotani, B., Lahiri, M., Marechal, A., Tse, A., Leung, C. C., Glover, J. N., Yang, X. H., and Zou, L. (2011) ATR autophosphorylation as a molecular switch for checkpoint activation. *Molecular cell* **43**, 192-202
44. Lee, J. H., and Paull, T. T. (2004) Direct activation of the ATM protein kinase by the Mre11/Rad50/Nbs1 complex. *Science* **304**, 93-96
45. Navadgi-Patil, V. M., and Burgers, P. M. (2009) A tale of two tails: activation of DNA damage checkpoint kinase Mec1/ATR by the 9-1-1 clamp and by Dpb11/TopBP1. *DNA repair* **8**, 996-1003
46. Pfander, B., and Diffley, J. F. (2011) Dpb11 coordinates Mec1 kinase activation with cell cycle-regulated Rad9 recruitment. *The EMBO journal* **30**, 4897-4907
47. Kumar, S., and Burgers, P. M. (2013) Lagging strand maturation factor Dna2 is a component of the replication checkpoint initiation machinery. *Genes & development* **27**, 313-321
48. Navadgi-Patil, V. M., and Burgers, P. M. (2008) Yeast DNA replication protein Dpb11 activates the Mec1/ATR checkpoint kinase. *J Biol Chem* **283**, 35853-35859

49. Navadgi-Patil, V. M., Kumar, S., and Burgers, P. M. (2011) The unstructured C-terminal tail of yeast Dpb11 (human TopBP1) protein is dispensable for DNA replication and the S phase checkpoint but required for the G2/M checkpoint. *J Biol Chem* **286**, 40999-41007
50. Guo, Z., Kozlov, S., Lavin, M. F., Person, M. D., and Paull, T. T. (2010) ATM activation by oxidative stress. *Science* **330**, 517-521
51. Majka, J., Niedziela-Majka, A., and Burgers, P. M. (2006) The checkpoint clamp activates Mec1 kinase during initiation of the DNA damage checkpoint. *Molecular cell* **24**, 891-901
52. Ludtke, S. J., Baldwin, P. R., and Chiu, W. (1999) EMAN: semiautomated software for high-resolution single-particle reconstructions. *Journal of structural biology* **128**, 82-97
53. Tang, G., Peng, L., Baldwin, P. R., Mann, D. S., Jiang, W., Rees, I., and Ludtke, S. J. (2007) EMAN2: an extensible image processing suite for electron microscopy. *Journal of structural biology* **157**, 38-46
54. Mindell, J. A., and Grigorieff, N. (2003) Accurate determination of local defocus and specimen tilt in electron microscopy. *Journal of structural biology* **142**, 334-347
55. van Heel, M., Harauz, G., Orlova, E. V., Schmidt, R., and Schatz, M. (1996) A new generation of the IMAGIC image processing system. *Journal of structural biology* **116**, 17-24
56. Scheres, S. H. (2012) RELION: implementation of a Bayesian approach to cryo-EM structure determination. *Journal of structural biology* **180**, 519-530
57. Scheres, S. H., and Chen, S. (2012) Prevention of overfitting in cryo-EM structure determination. *Nature methods* **9**, 853-854
58. Shaikh, T. R., Gao, H., Baxter, W. T., Asturias, F. J., Boisset, N., Leith, A., and Frank, J. (2008) SPIDER image processing for single-particle reconstruction of biological macromolecules from electron micrographs. *Nat Protoc* **3**, 1941-1974
59. Scheres, S. H. (2012) A Bayesian view on cryo-EM structure determination. *J Mol Biol* **415**, 406-418
60. Pettersen, E. F., Goddard, T. D., Huang, C. C., Couch, G. S., Greenblatt, D. M., Meng, E. C., and Ferrin, T. E. (2004) UCSF Chimera--a visualization system for exploratory research and analysis. *Journal of computational chemistry* **25**, 1605-1612
61. Paciotti, V., Clerici, M., Scotti, M., Lucchini, G., and Longhese, M. P. (2001) Characterization of mec1 kinase-deficient mutants and of new hypomorphic mec1 alleles impairing subsets of the DNA damage response pathway. *Mol Cell Biol* **21**, 3913-3925
62. Chan, D. W., Chen, B. P., Prithivirajsingh, S., Kurimasa, A., Story, M. D., Qin, J., and Chen, D. J. (2002) Autophosphorylation of the DNA-dependent protein kinase catalytic subunit is required for rejoining of DNA double-strand breaks. *Genes & development* **16**, 2333-2338
63. Soliman, G. A., Acosta-Jaquez, H. A., Dunlop, E. A., Ekim, B., Maj, N. E., Tee, A. R., and Fingar, D. C. (2010) mTOR Ser-2481 autophosphorylation monitors mTORC-specific catalytic activity and clarifies rapamycin mechanism of action. *J Biol Chem* **285**, 7866-7879

FIGURE LEGENDS

FIGURE 1. ***Purification of Mec1-Ddc2 and Tel1.*** (A) SDS-PAGE of Mec1-Ddc2. (B) Gel filtration profile of Mec1-Ddc2 indicating Mec1-Ddc2 exists as a dimer. The inlet shows the kinase activity for specific fractions as indicated from the gel filtration profile. (C) SDS-PAGE of Tel1. (D) Gel filtration profile of Tel1 indicating Tel1 exists as a dimer. V_0 represents the aggregated material.

FIGURE 2. ***Negative stain-EM 3D reconstruction of Mec1-Ddc2 dimer.*** (A) A representative micrograph of negatively stained Mec1-Ddc2 particles. (B) A comparison between 2D class averages (CA) and their corresponding reprojections (RP) generated from the negative stain 3D model. Scale bars in (A) and (B) correspond to 200 Å. (C) Different views of the 3D negative stain structure of Mec1-Ddc2 dimer. Left panel shows the side view, middle panel shows the front view and the upper and lower right panels show

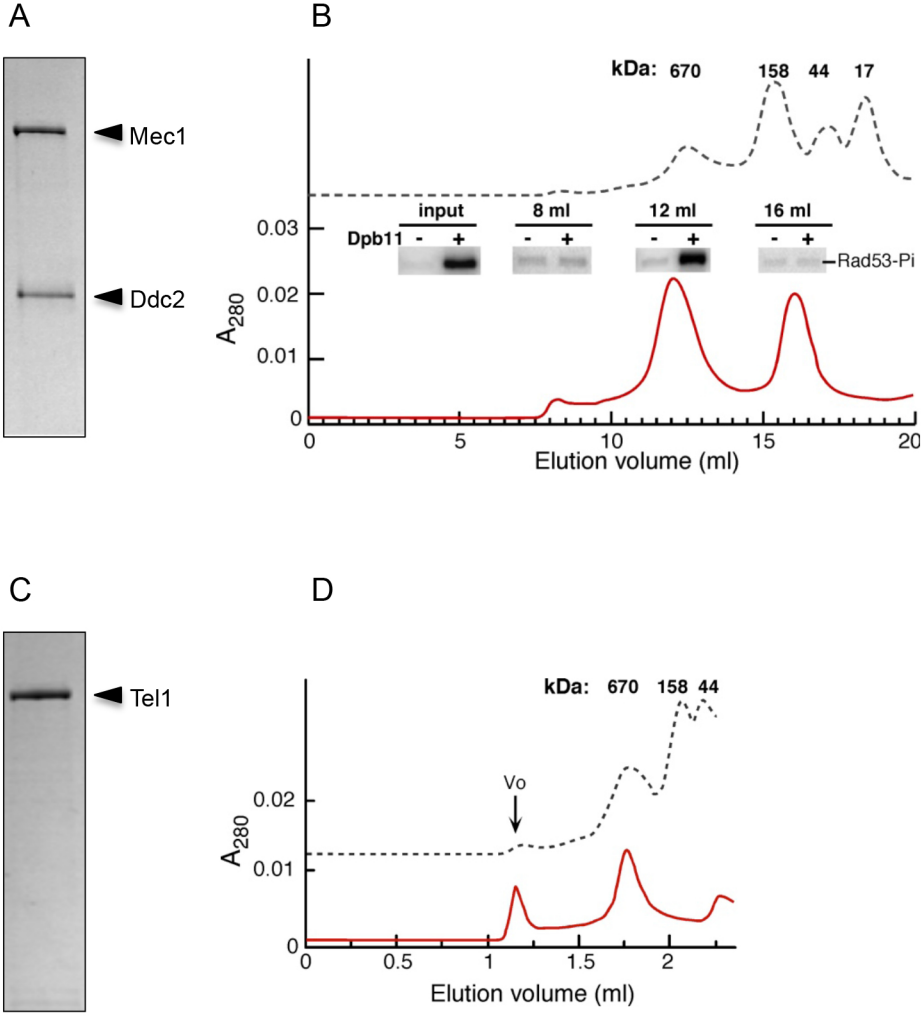
top and bottom views, respectively. (D) Euler angle distribution of all particles used in refinement of the C2 symmetrized 3D model. (E) Fourier Shell Correlation curve used to calculate the model resolution of 22.5 Å according to the gold-standard FSC (0.143 criterion).

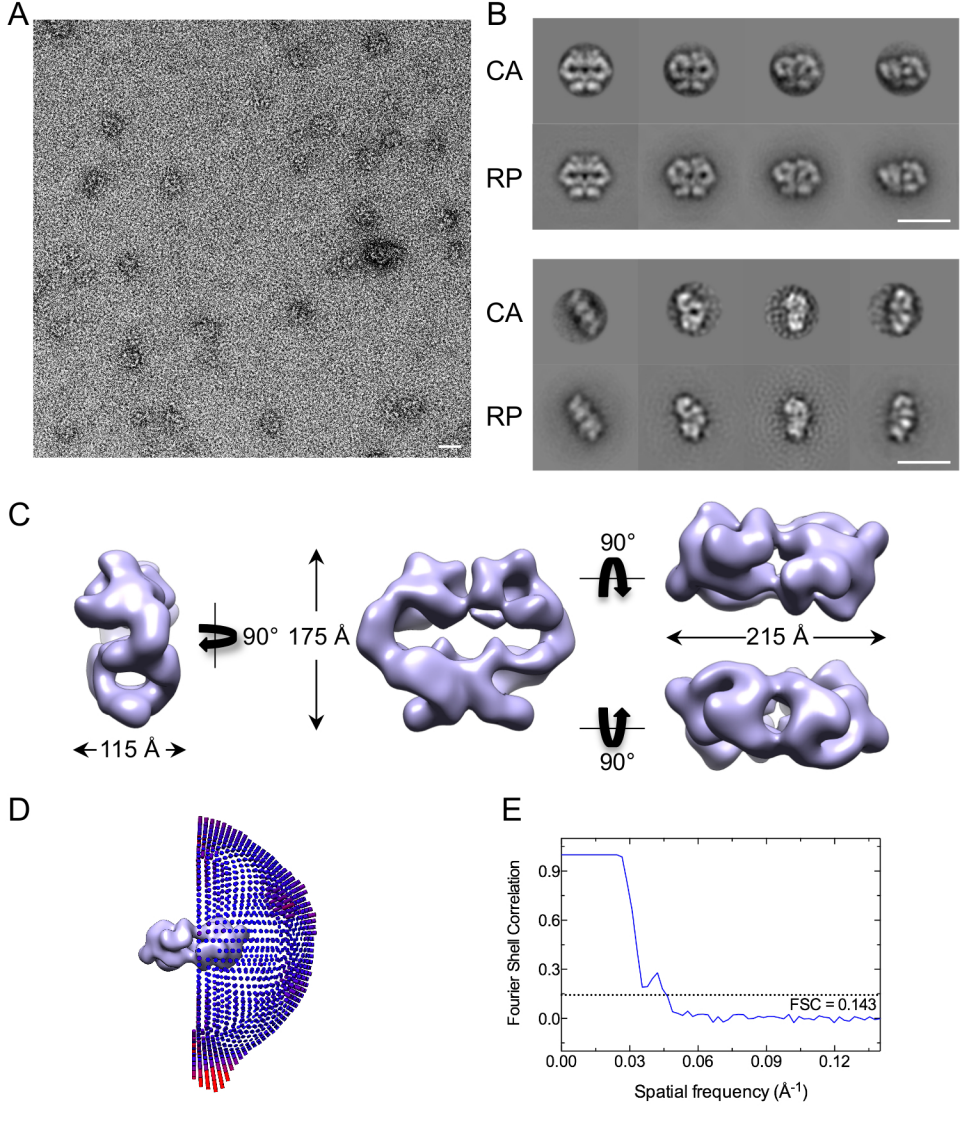
FIGURE 3. ***Negative stain-EM 3D reconstruction of Tel1 dimer.*** (A) A representative micrograph of negatively stained Tel1 particles. (B) A comparison between 2D class averages (CA) and their corresponding reprojections (RP) generated from the negative stain 3D model. Scale bars in (A) and (B) correspond to 200 Å. (C) Different views of the 3D negative stain structure of Tel1 dimer. Left panel shows the side view, middle panel shows the front view and the upper and lower right panels show top and bottom views, respectively. (D) Euler angle distribution of all particles used in refinement of the C2 symmetrized 3D model. (E) Fourier Shell Correlation curve used to calculate the model resolution.

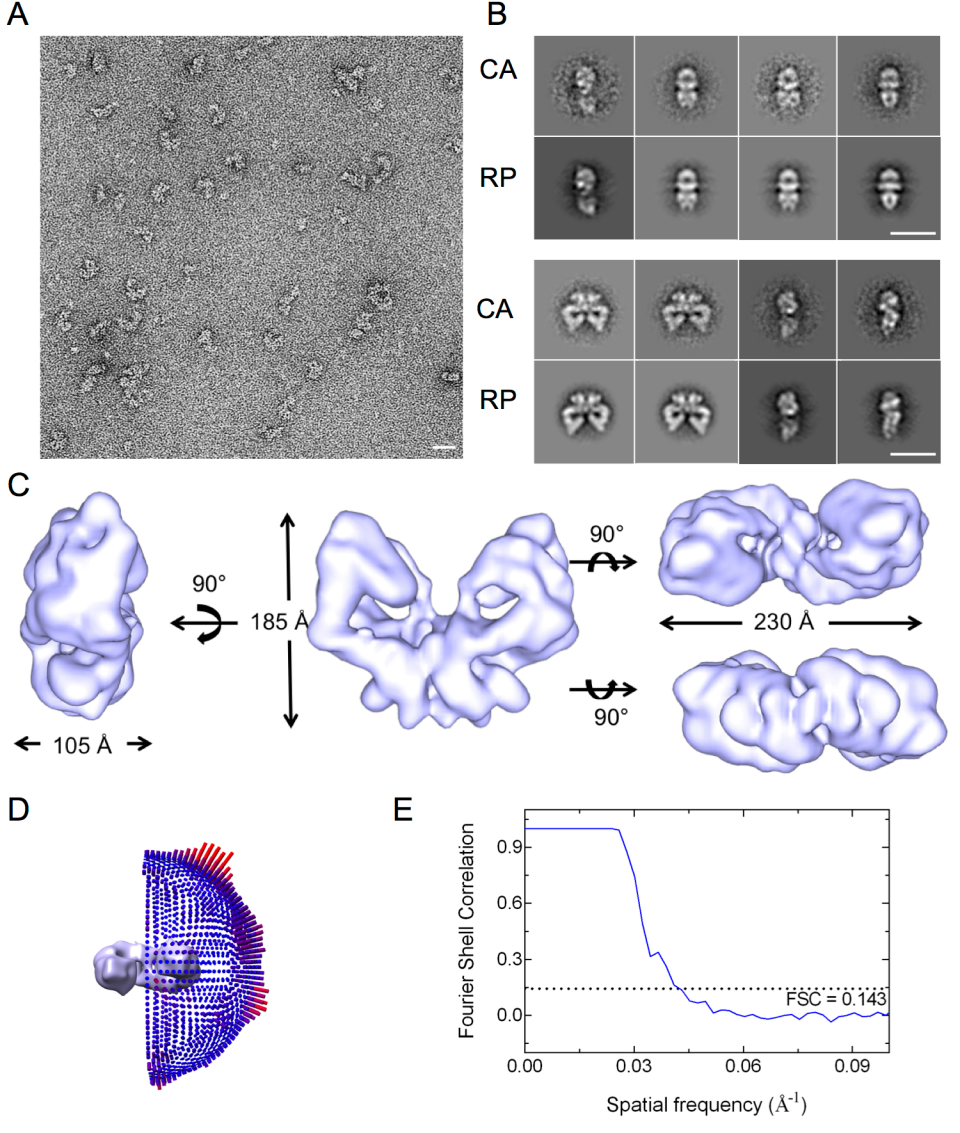
FIGURE 4. ***Cryo-EM 3D reconstruction of Tel1 dimer***. (A) A representative micrograph of cryo-frozen Tel1 particles on carbon coated grids. (B) A comparison between 2D class averages (CA) and their corresponding reprojections (RP) generated from the 3D model. Scale bars in (A) and (B) correspond to 200 Å. (C) Different views of the 3D negative stain structure of Tel1 dimer. Left panels show the side views, middle panel shows the front view and the upper and lower right panels show top and bottom views, respectively. (D) Euler angle distribution of all particles used in refinement of the non-symmetrized 3D model. (E) Fourier Shell Correlation curve used to calculate the model resolution of 19.2 Å according to the gold-standard FSC (0.143 criterion).

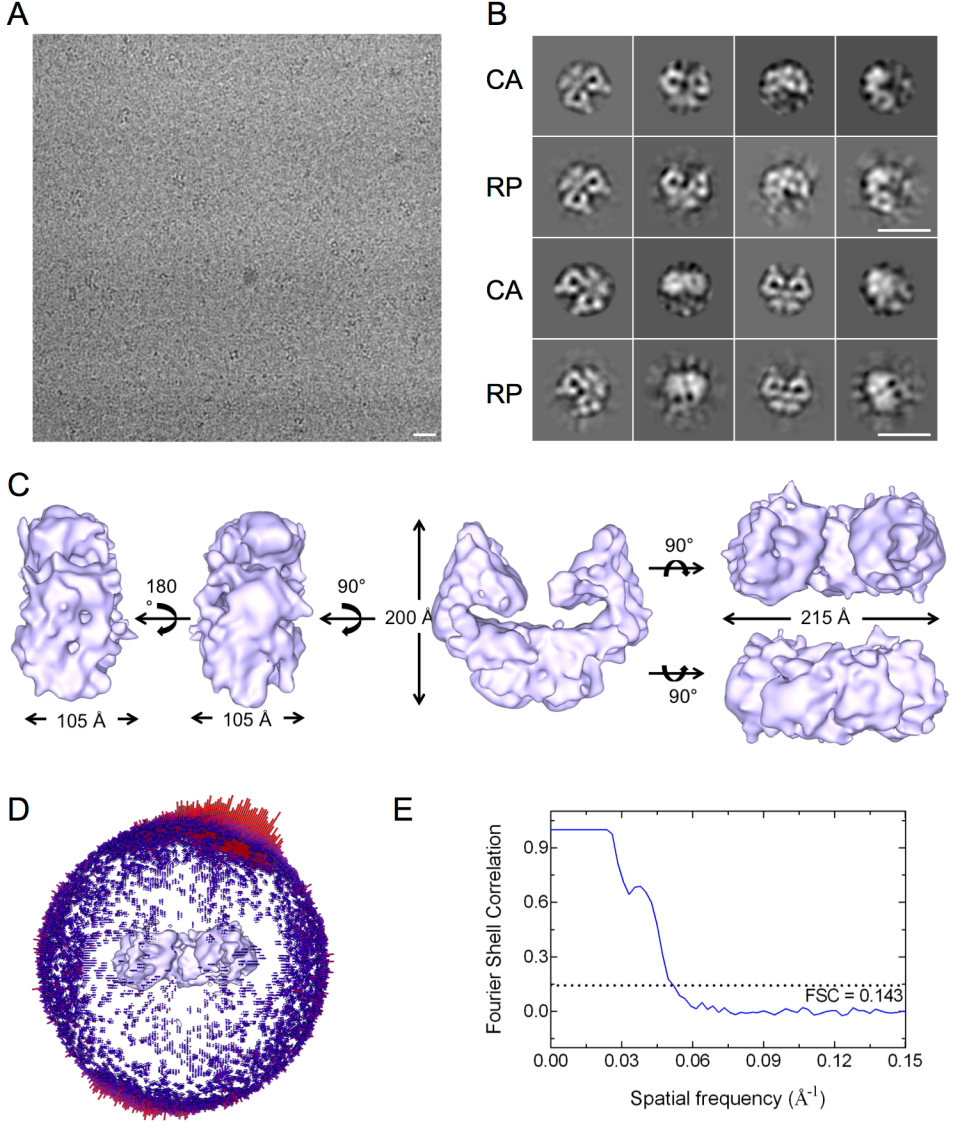
FIGURE 5. ***Antibody labelling of the Mec1-Ddc2 and Tel1 reconstructions.*** (A) Antibody labelling against the C-terminus of Mec1. Class averages (CA) of anti-FATC antibody labelled Mec1-Ddc2 show a clear extra density highlighted by white arrows. The density is missing in reprojections (RP) generated from the unlabelled Mec1-Ddc2 dimeric model along the same Euler angles as assigned to CA. Magenta markers indicate the location of the anti-FATC antibody as shown by surface views (SV) of Mec1-Ddc2 along the same Euler angles as in CA and RP. (B) Antibody labelling against the C-terminus of Tel1. Individual particles (IP) show a clear extra density highlighted by white arrows. The density is missing in reprojections (RP) generated from the unlabelled Tel1 dimeric model along the same Euler angles as assigned to IP. Magenta markers indicate the location of the anti-FATC antibody as shown by surface views (SV) of Tel1 along corresponding angles. Scale bars correspond to 200 Å.

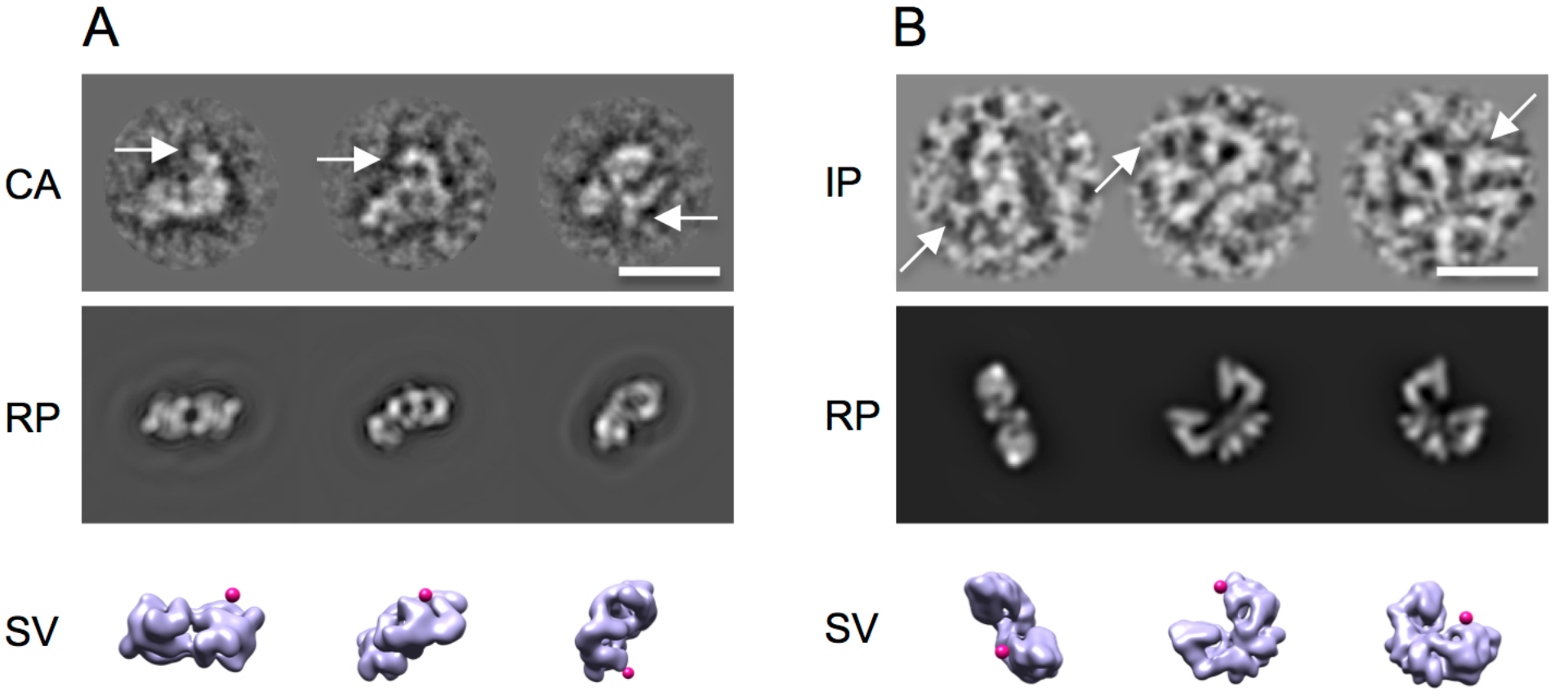
FIGURE 6. ***Comparison of Mec1-Ddc2, Tel1 and mTORC1***. (A) Schematic domain arrangement of Ddc2, Mec1, Tel1 and mTOR. (B) Top and front views of the Mec1-Ddc2 EM reconstruction and (C) Top and front views of the Tel1 EM reconstruction with mTOR structures fitted in as well as the top and front views of the segmented maps based on domain locations. FATC and Kinase domain – pink, FAT and HEAT repeats – cyan, N-terminal HEAT repeats – dark blue. The extra tubular density in Mec1-Ddc2 compared to Tel1, which accounts for Ddc2, is shown in green. (D) Top and front views of the atomic model of mTOR (PDB ID: 5FLC) fitted into the 5.9 Å cryo-EM structure of mTORC1 (EMD-3213). Densities corresponding to Raptor and mLST8 subunits of the complex as well as the FKBP protein have been removed. Top and front views of the segmented map of mTOR. Red stars indicate the position of the active sites.

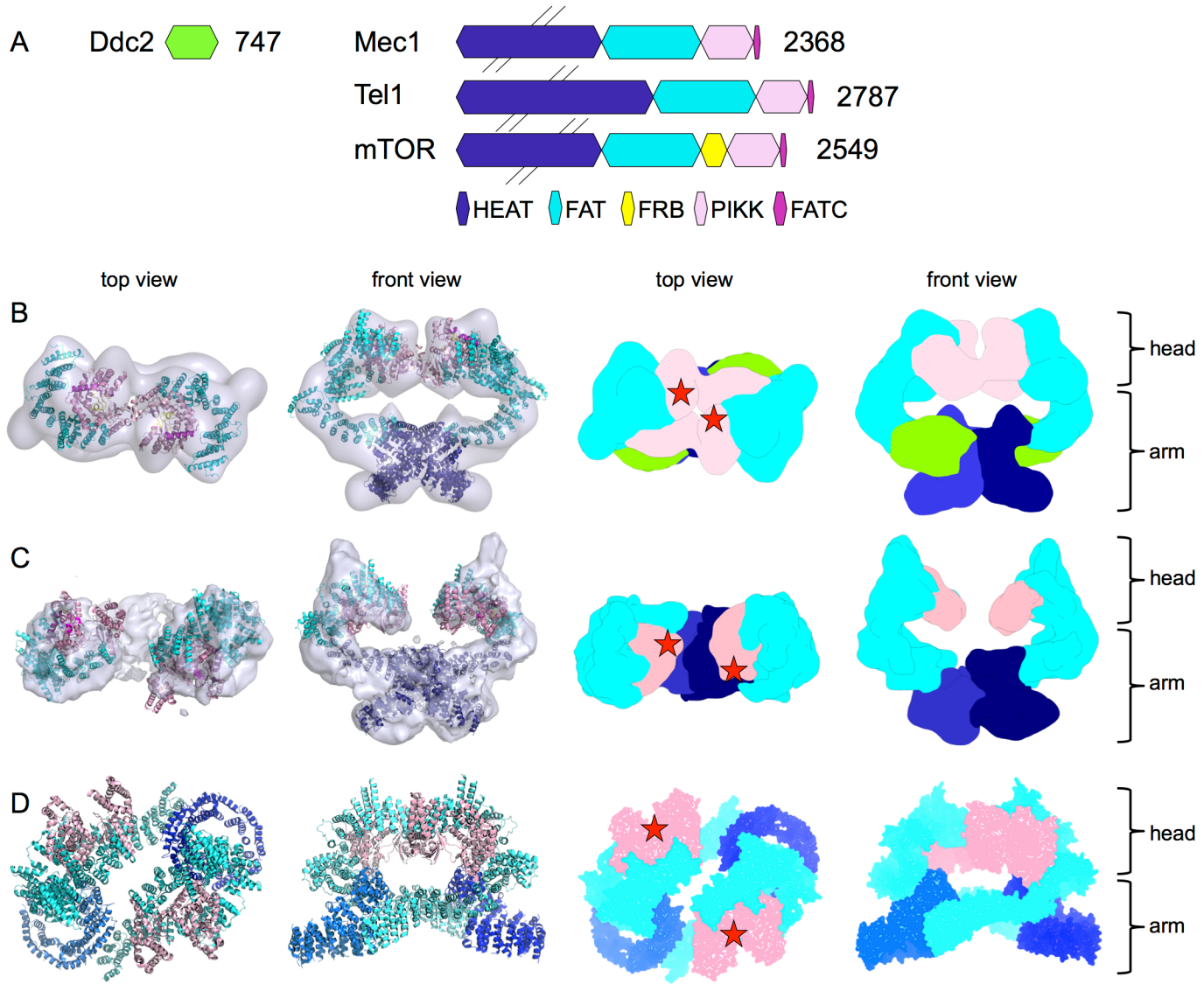

A
Mec1
Ddc2
B
kDa: 670 158 44 17
input
8 ml
12 ml
16 ml
Dpb11 - + - + - + - +
Rad53-Pi
A280
0.03
0.02
0.01
0
0 5 10 15 20
Elution volume (ml)
C
Tel1
D
kDa: 670 158 44
Vo
A280
0.02
0.01
0
0 0.5 1 1.5 2
Elution volume (ml)


A
B
CA
RP
CA
RP
C
90°
175 Å
115 Å
90°
215 Å
90°
D
E
Fourier Shell Correlation
0.9
0.6
0.3
0.0
FSC = 0.143
0.00
0.03
0.06
0.09
0.12
Spatial frequency (Å-1)


A
B
CA
RP
CA
RP
C
90°
185 Å
105 Å
90°
230 Å
90°
D
E
Fourier Shell Correlation
0.9
0.6
0.3
0.0
FSC = 0.143
0.00
0.03
0.06
0.09
Spatial frequency (Å^{-1})


A
B
CA
RP
CA
RP
C
180°
90°
200 Å
90°
90°
215 Å
105 Å
105 Å
D
E
Fourier Shell Correlation
0.9
0.6
0.3
0.0
FSC = 0.143
0.00
0.03
0.06
0.09
0.12
0.15
Spatial frequency (Å^{-1})


A
CA
RP
SV
B
IP
RP
SV


A
Ddc2
747
Mec1
2368
Tel1
2787
mTOR
2549
HEAT
FAT
FRB
PIKK
FATC
top view
front view
top view
front view
B
head
arm
C
head
arm
D
head
arm